communications earth & environment

Article

A Nature Portfolio journal

https://doi.org/10.1038/s43247-025-02071-0

Narrow intermediate-depth seismogenic band related to flexural strain in relatively dry Peruvian flat slab

Lingci Zeng [1,2], Lingling Ye [2,3] ✉, Huajian Yao [1,4,5] ✉, Wei Liu [2], Daojun Si[2], Thorne Lay [6] & Ting Yang [2,3]

The distribution and rupture properties of intermediate-depth earthquakes (70–300 km) provide insights into the interior stress state of the subducting plate, its petrological composition, and the subduction history. Here we evaluate the kinematic spatio-temporal rupture evolutions of four *M*7+ intermediate-depth earthquakes beneath Peru between 1997 and 2021 using teleseismic waveforms, which reveal similar rupture behavior over a limited depth range within the flat-slab segment. The intermediate-depth seismogenic zone is confined within a narrow band ~20 km thick near the slab surface, as also found in Pampean and Mexican flat slabs, contrasting to the broader seismicity distributions in the adjacent normally-dipping segments. The elongated earthquake ruptures in flat slabs with few aftershocks and the narrow, sparse seismicity bands are attributed to flexure from along-dip slab steepening and limited dehydration reactions within relatively dry flat-slab segments. Conversely, the diffuse seismicity in adjacent normally-dipping segments is likely associated with more widespread dehydration reactions.

Intraslab seismic activity is related to plate tectonics and subduction history[1–4]. The slab-pull and plate bending associated with the subduction process result in internal slab extension, while the resistance from the surrounding mantle and plate unbending lead to internal slab compression, reflected in the systematically oriented down-dip extensional or compressional principal stress axes of intraslab seismicity in subduction zones[3–5]. Within the subducting slab at depths of 70–300 km, intermediate-depth seismicity is generally considered to be primarily triggered by dehydration reactions because these earthquakes tend to concentrate below arc volcanoes[6]. Dehydration reactions take place progressively, inducing pore fluid overpressure for antigorite-rich material if the volume change is positive[7–10], thus decreasing effective normal stress and triggering brittle shear failures, as observed in serpentinized peridotites[11]. For lower amounts of antigorite at higher pressure (>2 GPa) where the volume change is negative, fluid overpressure may not develop and it is proposed that dehydration stress transfer may trigger embrittlement[9,10]. However, the traditional understanding of intermediate-depth seismicity has been challenged by the occurrence of major earthquakes within flat slabs beneath Mexico and Peru given the unique mechanical and metamorphic conditions of the slab geometry and dynamic evolution[12–15].

Major intermediate-depth earthquakes occur infrequently, with less than 200 *M*7+ intermediate-depth events recorded worldwide since 1900. Most of these large intermediate-depth earthquakes have struck in the western Pacific where subducting slabs are old and cold, but some do occur in the relatively young and warm subduction regions beneath South America and Mexico. Although less frequent and deeper underground than shallow events, intermediate-depth earthquakes can still lead to major disasters. For example, the ~80–90 km deep 1939 M_S 7.8 earthquake in central Chile took ~28,000 lives[16], exceeding the death tolls of the M_W 9.5 shallow southern Chile earthquake in 1960 or the 2011 Tohoku-Oki earthquake and subsequent tsunami (<23,000). The 2017 M_W 8.2 Chiapas earthquake at 58 km depth occurred within the slab bend and broke the entire underthrust Cocos lithosphere[14], causing about 100 fatalities and damaging 41,000 homes in Chiapas[17]. The 2017 M_W 7.1 Puebla earthquake (~60 km depth) near the end of a nearly horizontal slab segment caused huge ground motion, damaging over 15,000 buildings and killing 369 people

[1]Laboratory of Seismology and Physics of Earth's Interior, School of Earth and Space Sciences, University of Science and Technology of China, Hefei, China. [2]Department of Earth and Space Sciences, Southern University of Science and Technology, Shenzhen, China. [3]Guangdong Provincial Key Laboratory of Geophysical High-resolution Imaging Technology, Southern University of Science and Technology, Shenzhen, China. [4]Mengcheng National Geophysical Observatory, University of Science and Technology of China, Mengcheng, China. [5]CAS Center for Excellence in Comparative Planetology, University of Science and Technology of China, Hefei, China. [6]Department of Earth and Planetary Sciences, University of California Santa Cruz, Santa Cruz, CA, USA. ✉e-mail: yell@sustech.edu.cn; hjyao@ustc.edu.cn

in Mexico City[14]. These events involved normal faulting in the subducting slab, possibly associated with stress concentration from localized steepening of the slab dip[14,17,18].

Large intermediate-depth earthquakes can involve substantial slip and extensive rupture areas. The 2014 M_W 7.9 Rat Islands earthquake (~100 km depth) broke across the cold core of the underthrust slab, possibly due to stress accumulation from slab bending and relative plate motions. The lateral extent of the rupture was delimited by pre-existing slab heterogeneity such as the subducted Rat fracture zone and a lithospheric tear below the Amchitka Pass[19,20]. The 26 May 2019 M_W 8.0 northern Peru earthquake (hypocenter ~123 km deep), the largest intermediate-depth earthquake recorded by modern seismometers, occurred near an abrupt steepening at the down-dip end of a wide flat-slab segment with anomalously few aftershocks. The sparse aftershock activity is attributed to a relatively homogeneous medium under uniform stress distribution within the flat slab[21]. The stress and strain regimes of the plate interior thus play an important role in the occurrence and propagation of intermediate-depth seismicity[15,22–27].

Among three major present-day flat subduction regions along the east Pacific subduction zones, the Mexican flat-slab segment[28], the Peruvian flat-slab segment[29], and the Pampean flat-slab segment of central Chile and Argentina[29], the Peruvian flat-slab segment provides a particularly promising source region for further investigation, with several recent major intermediate-depth earthquakes that are well recorded by global broadband seismic data. In this study, we quantify the rupture process for four $M7+$ earthquakes in the Peruvian flat-slab segment in 1997, 2005, 2019, and 2021 to evaluate the spatial extent of the brittle failure in the flat slab. Along with a systematic investigation of the relative spatial extent of intermediate-depth seismicity beneath South America and Mexico within both flat and normally-dipping slabs, we find a narrow seismogenic band for earthquake occurrence and rupture propagation in flat slabs that might result from the differential stress due to the flexural strain as the slab re-steepens. We do not address specific triggering mechanisms of the faulting as we focus on the seismic observations, but we do note independent evidence for the relative extent of dehydration in the flat slabs.

Results

Elongated ruptures for major earthquakes in the Peruvian flat slab

The 27 October 1997 M_W 7.2, 25 September 2005 M_W 7.5, 26 May 2019 M_W 8.0, and 28 November 2021 M_W 7.5 major intermediate-depth earthquakes beneath Peru all occurred in the subducting Nazca plate toward the eastern end of the ~450 km wide flat-slab segment, within 100 km from where the slab abruptly steepens. They all show a deficiency of aftershocks[21], with, respectively, 0, 1, 3, and 4 detected intermediate-depth aftershocks whose magnitude ranges from M_W 4.1 to M_W 4.9 within 45 days from the USGS-NEIC catalog (https://www.usgs.gov/programs/earthquake-hazards/earthquakes; the catalog completeness for this region is $M_W \sim 4.5$). Both the USGS-NEIC catalog and our relative locations (see Methods: Hypocenter relocation) indicate that most intraslab events occur toward the eastern end of the wide Peruvian flat-slab segment within a narrow depth range of 100–140 km (Figs. 1, S1–S4). All the intermediate-depth events from the Global Centroid Moment Tensor (GCMT; https://www.globalcmt.org) catalog within the Peruvian flat slab have normal faulting focal mechanisms with nearly parallel quasi-horizontal tension axes, indicating relatively uniform stress within this flat slab.

Seismological data indicate that three of the four major earthquakes have ruptures extending along the strike, characterized by predominantly unilateral ruptures. The previously studied 2019 M_W 8.0 event ruptured ~170 km along strike to the NNW (Fig. 1b) with an average rupture speed of ~3 km s^{-1}[21]. The 1997 M_W 7.2 (hypocenter ~112 km deep) and the 2021 M_W 7.5 (~126 km deep) earthquakes show directivity to the SSE at reference rupture directions of $\varphi_{ref} = 157°$ and $\varphi_{ref} = 146°$, respectively, along a pair of nearly parallel faults (Figs. 2a, c, S5, and S7). The peak slip of the 1997 M_W 7.2 earthquake is located ~23 km from the epicenter at ~8.8 s, indicating a rupture speed of ~2.6 km s^{-1}. The peak slip of the 2021 M_W 7.5 earthquake is located ~61 km away to the SSE at ~14.5 s after the first arrival, indicating an average rupture speed of ~4.2 km s^{-1}. A compressive-sensing back-projection (CS-BP) analysis of the coherent high-frequency (HF; 0.7–2.0 Hz; Fig. S8) signals[30] shows that the 2021 M_W 7.5 earthquake extends unilaterally ~60 km along the SSE direction in ~15 s (Fig. 3b2 and c2). The HF energy radiation mainly concentrates in two regions: near the epicenter and at ~40–60 km to the SSE. The average rupture speed is ~3.5 km s^{-1}, somewhat lower than the estimate from broadband P wave ground displacements.

The 2005 M_W 7.5 earthquake (~115 km deep) shows weak eastward along-dip directivity with a reference rupture direction of $\varphi_{ref} = 85°$ with the peak slip located ~18 km away from the epicenter at ~4.9 s, indicating an average rupture speed of ~3.7 km s^{-1} (Figs. 2b and S6). The CS-BP results show an asymmetric bilateral rupture extending ~25 km toward the NE, with an average rupture speed of ~4.0 km s^{-1} (Fig. 3b1 and c1), comparable to the directivity analysis of broadband P-wave ground displacements.

The coseismic slip distributions revealed by finite-fault inversions of teleseismic P-wave recordings show that all four $M7+$ earthquakes in the Peruvian flat slab involve slip within a narrow depth range of ~110–139 km. We consider the slip distribution on both fault planes and choose the eastward-dipping fault planes for the 1997, 2005, and 2021 earthquakes as our preferred fault planes following Ye et al.[21], who find that the eastward-dipping fault plane for the 2019 M_W 8.0 earthquake is consistent with the high-frequency seismic radiation. Our slip model for the 1997 M_W 7.2 earthquake shows a unilateral along-strike rupture, which propagates southeastward ~35 km in ~12 s, with large-slip patches located at depths of ~112–132 km (Fig. 4). The 2005 M_W 7.5 earthquake has a down-dip rupture expansion, propagating ~40 km along the dip direction in ~13 s with the peak slip of ~2.7 m located ~18 km east of the hypocenter (Fig. 5). Despite the down-dip rupture propagation, the large-slip patch is still concentrated within a fairly narrow depth range of ~110–139 km. Our slip model for the 2021 M_W 7.5 earthquake indicates a smooth and simple unilateral rupture along strike (Fig. 6), similar to the 1997 event. It extends ~60 km towards the SSE with large-slip patches at depths of ~116–132 km. Our slip models for all these 3 major earthquakes are consistent with the directivity analysis and the evolution of HF radiations (Fig. 7). Multiple peaks in the source time functions of the 1997 and 2021 earthquakes resulting from several slip patches and two clusters of concentrated HF radiation during the 2021 rupture indicate rupture heterogeneity. The single-peak moment rate function for the 2005 M_W 7.5 earthquake reflects its simple and continuous rupture as indicated by the distribution of slip and HF radiation. Our slip models fit depth phases well (Figs. 4–6), demonstrating the reliability of depth distribution of slip. Slip models on the alternative westward-dipping nodal planes show similar slip patterns with large-slip patches again restricted to narrow depth ranges (Figs. S10–S13).

The 1997, 2005, and 2021 earthquakes share similar rupture characteristics with the 2019 M_W 8.0 earthquake[21,31–33]. The 1997 M_W 7.2, 2019 M_W 8.0, and 2021 M_W 7.5 earthquakes all have along-strike ruptures propagating within relatively narrow depth ranges, consisting of two or three major slip patches removed from the hypocenter (Fig. 7). They have comparable dimensions for the large-slip patch, rupture velocities (~3.0 km s^{-1}), and stress drops (2.0–4.5 MPa, Table S1). Such stress drop values are also typical for global major events[34], for similarly parameterized rupture models, all of which have uncertainties in slip distributions. The source spectra for the 1997, 2005, 2019, and 2021 events are all enriched in HF radiation compared to the reference ω^{-2} spectrum (Fig. 7b–e). The moment-scaled radiated energy E_R/M_0 values are $2.2 - 4.7 \times 10^{-5}$ (Table S1), which are typical for intermediate-depth and deep-focus earthquakes[35–38] and relatively high compared with global major events[34]. The relatively high moment-scaled radiated energy and rupture velocities (with typical stress drops) indicate relatively low dissipating rupture processes with radiation efficiencies larger than 0.5 (Table S1), in contrast to the extremely low radiation efficiency observed for moderate earthquakes in the Bucaramanga Nest[39]. The uniform focal mechanisms in the Peruvian flat slab (Fig. 1), the lack of moderate-size aftershocks for all the four major earthquakes (Fig. 7f), and the close proximity of aftershocks with main slip

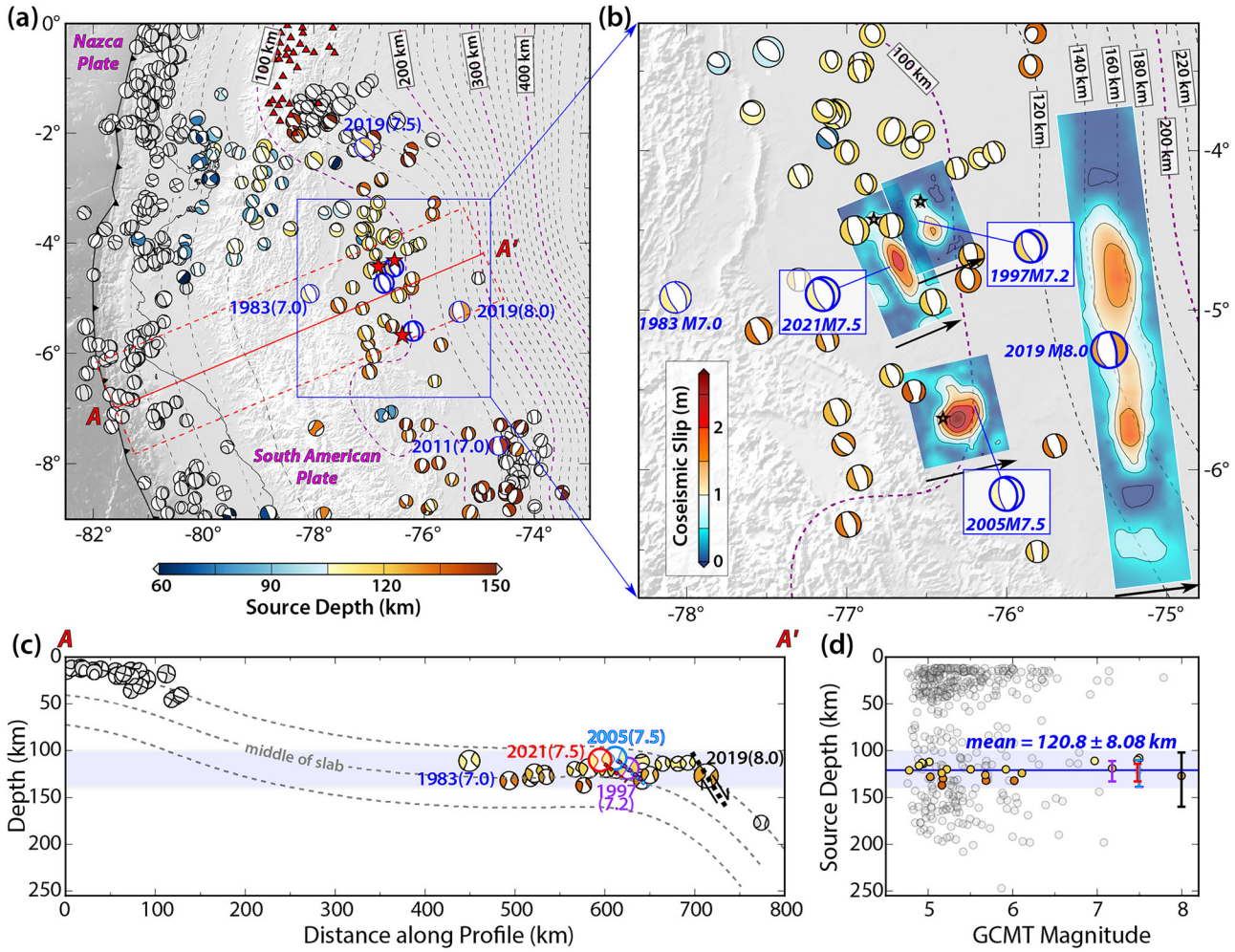

Fig. 1 | Large intermediate-depth earthquakes and seismicity under Peru. a Three relocated major intermediate-depth earthquakes (red stars) in 1997, 2005, and 2021, along with focal mechanisms since 1976 from the Global Centroid Moment Tensor (GCMT) catalog, shown at the centroid locations. Events 60–150 km deep are color-coded with source depth; seismicity in the South American Plate has been removed. Red triangles show volcano locations. Purple and gray dashed curves show slab contours with 20-km intervals from Slab 2.0 [52]. **b** Slip distributions of the 1997 M_W 7.2, 2005 M_W 7.5, 2021 M_W 7.5, and 26 May 2019 M_W 8.0 [31] earthquakes. The black arrows show the dip directions of preferred fault planes. **c** The depth profile of seismicity along AA' in (**a**) within the rectangle area outlined by the red dashed line. The rupture extent and preferred fault plane for the 2021, 2005, 1997, and 2019 [31] earthquakes are indicated by the red, cyan, purple, and black dashed lines with slip vectors, respectively. **d** Centroid depth distribution versus earthquake magnitudes for seismicity within the large-scale tectonics region in (**a**) from the GCMT catalog. Color-coded dots highlight those earthquakes in the flat slab along AA' in (**c**). The purple, red, cyan, and black bars indicate depth extent for the 1997, 2021, 2005, and 2019 ruptures, respectively.

patches (Fig. 7g) indicate a relatively homogeneous structure and uniform stress state for earthquake nucleation and propagation in the flat-slab[21].

Narrow flat-slab seismicity vs. widespread normally-dipping slab seismicity

The distance from seismicity to the slab surface is critical for identifying the viable mechanisms for intermediate-depth earthquakes because the pressure, temperature, and corresponding mechanical and metamorphic conditions change in the slab-normal direction, with the most abrupt variation near the slab surface. Seismicity at intermediate depths tends to be located in the cold upper half of the slab, mainly within the subducted crust and the uppermost mantle. Spatial correlation between the seismicity distribution and slab thermal structure from numerical simulation indicates that the seismicity is likely temperature-controlled and earthquakes occur within the cold part of the slab[40–44]. Widely observed double seismic zones[45–47] have been associated with different temperatures and dehydration processes for variable hydrous minerals, such as antigorite, chlorite, Phase A, and others[8,10,48]. The mechanism for the lower seismicity zone is still under debate, including embrittlement from the antigorite dehydration[7–9,49], transformation-driven stress transfer from slightly-serpentinized mineral destabilizations without fluid overpressure[10,50], and plastic deformation of anisotropic shear zones in the anhydrous mantle[51]. For flat slabs, Sandiford et al.[15,24] correlate seismicity and earthquake principal stress orientation with bending rate from numerical simulations and find that the flat-slab seismicity is primarily controlled by slab flexure. However, these analyses depend on robust constraints on the slab surface position and high-resolution seismic catalog, which are usually unavailable, and problematically, the slab surface position is typically inferred from the earthquake location (Slab 2.0[52]).

We analyze the minimum distances from intraslab earthquakes to the slab surface (Slab 2.0) beneath South America and Mexico, spanning three flat-slab sections and adjacent normally-dipping segments that have comparable seafloor age and convergence rate (Fig. S14). Using the well-relocated $M4.5+$ (this is the completeness level) hypocenters from the declustered ISC-EHB catalog (Figs. S15–S18; see Methods: seismicity distribution analysis), profiles AA' and BB' across the Peruvian flat-slab segment and Profile CC' across the Pampean flat-slab segment exhibit sparse seismicity, concentrated near the slab surface, in contrast to the continuous and widely distributed seismicity in profile DD' across the normally-dipping

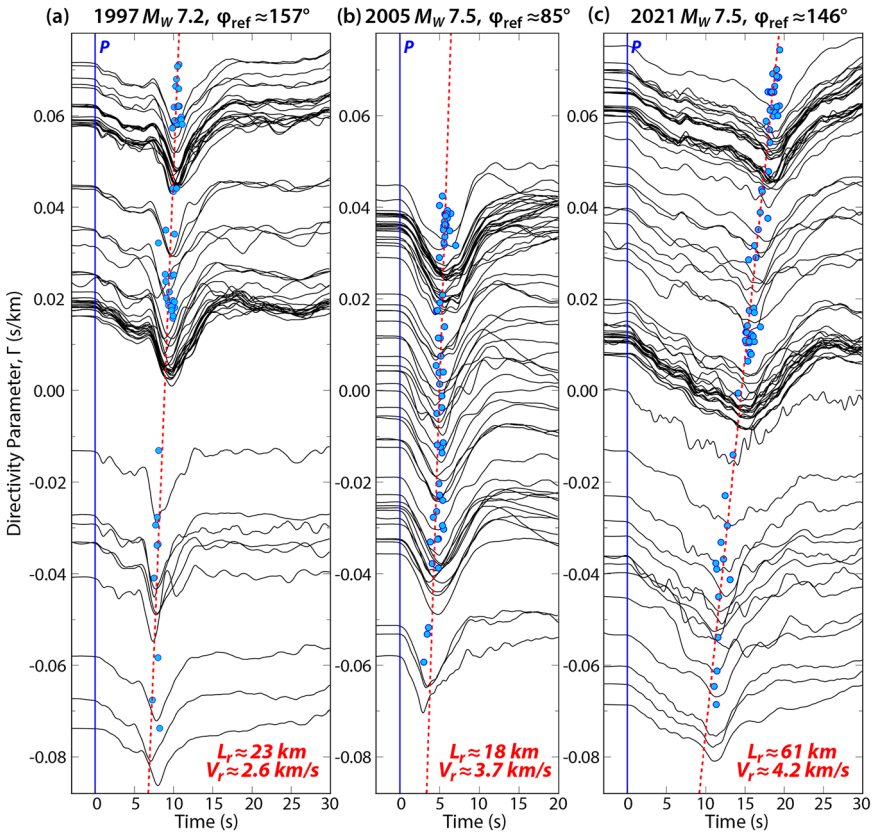

Fig. 2 | Directivity analysis for the 1997 M_W 7.2, 2005 M_W 7.5, and 2021 M_W 7.5 earthquakes beneath Peru. The P wave ground displacement waveforms are ordered by directivity parameter with reference rupture directions φ_{ref} of 157°, 85°, and 146° for **a** the 1997 M_W 7.2, **b** the 2005 M_W 7.5, and **c** the 2021 M_W 7.5 earthquakes, respectively. The blue dots indicate the peak displacement time and directivity parameter at the corresponding stations. Red dashed lines fitting the broadband displacement peaks (blue dots) indicate the reference rupture direction, rupture length, and rupture speed obtained by L2-norm inversion (see Figs. S5–S7).

subduction region (Fig. 8a). In these flat-slab regions, intraslab seismicity terminates where the slab steepens at ~200 km depth, while adjacent normally-dipping slab seismicity extends to greater depths. Similar patterns are observed within the Mexican flat-slab segment and nearby normally-dipping slab segments (Fig. 8b). Of course, analysis of the distance of seismicity to the slab surface strongly depends on the slab boundary position. With a lack of high resolution in seismicity absolute location, there is large uncertainty in calculating seismicity-to-slab surface distances.

To reduce the sensitivity to slab geometry, we develop a statistical approach focusing on the range and variance of the seismicity-to-slab surface distances, corresponding to a relative distribution of seismicity in the slab-normal direction. The relative distribution mitigates the influence of inaccurate seismicity and slab boundary locations, thereby providing a more accurate depiction of the systematic variation in width of the seismicity distribution. We find distinct seismicity distributions within flat-slab segments compared to adjacent normally-dipping segments beneath South America and Mexico (Figs. 9 and S19). Beneath South America, most intermediate-depth seismicity occurs ~10–30 km below the surface of the subducting Nazca slab with a relatively uniform and broad distribution. However, intraslab earthquakes within the Peruvian and Pampean flat-slab segments, analyzed for a 0.3° averaging grid, are limited within ~10 km, in contrast to the wide distribution range of ~20–25 km within the normally-dipping regions. The pattern is rather stable with little dependence on grid size or interpolation (Fig. S20). We observe a rather similar seismicity distribution beneath Mexico where the subducting Cocos plate flattens at a shallower depth of ~50 km. The seismicity in the Mexican flat-slab segment mainly occurs near the slab surface, within a narrow distribution range of ~10 km, while that in the adjacent normally-dipping slab distributes over a broader range with a width of ~20–30 km (Figs. S19 and S21).

Discussion and conclusion

Narrow intermediate-depth seismogenic band within flat slabs

The rupture extent of four $M7+$ intermediate-depth earthquakes and the seismicity distribution jointly suggest a narrow seismogenic band within the flat-slab segment beneath Peru. The similar pattern of the seismicity distribution in different subduction regions beneath South America and Mexico indicates that the narrow seismogenic band is a robust feature for flat slabs, distinct from adjacent normally-dipping segments with similar age. It's worth mentioning that the source depths of the Peruvian intraslab seismicity (~95–140 km) correspond to the events that are inferred to be facilitated by dehydration reactions with negative volume change (e.g. ref. 53), as revealed by stress fields in the Vrancea slab[54]. Previous studies show that the seismogenic width for such dehydration reaction is about the same for given slab age (e.g. refs. 50,53). However, the flat slabs have comparable ages (Fig. S14) but distinct seismogenic widths (Figs. 9 and S19) with their adjacent normal slabs. The South American flat slabs (30–40 Myr) and the Mexican flat slabs (~13 Myr) have seismogenic layers with almost the same thickness, indicating properties influenced by their common slab geometry. Another point is that the rupture direction of the 2005 M_W 7.5 earthquake differs from that of the other large Peruvian earthquakes. As it occurred near the southern transition between the flat- and normally-dipping segments, along-strike southward rupture was likely prevented by the change in plate geometry, leading to down-dip rupture expansion distinct from the other large earthquakes in the flat slab, but its rupture depth extent did not obviously increase.

The widespread seismicity in normally-dipping subducting slabs may be associated with the dehydration of various mantle minerals enabled by the variation of P-T conditions within the subducting slab (e.g. refs. 7,8,50,55,56). A broad double seismic zone has been recognized between ~20°S–24°S in the normally-dipping subduction region beneath northern Chile[47,57]. With the velocity structure revealed by local observations in northern Chile, Dorbath et al.[58] find that the intraslab seismicity within the normally-dipping section occurs in regions with a broad range of V_P/V_S (~1.57–1.80). In the subduction zone, various hydration phases can exist alongside serpentine minerals (e.g., antigorite) at different conditions, such as talc (4.7 wt.%, <710 °C at 4.6 GPa[59]), brucite (~15 wt.%, <500 °C[8]), and chlorite (~13 wt.%, <700 °C[60]), as well as lawsonite (11.5 wt.%, ~400–600 °C

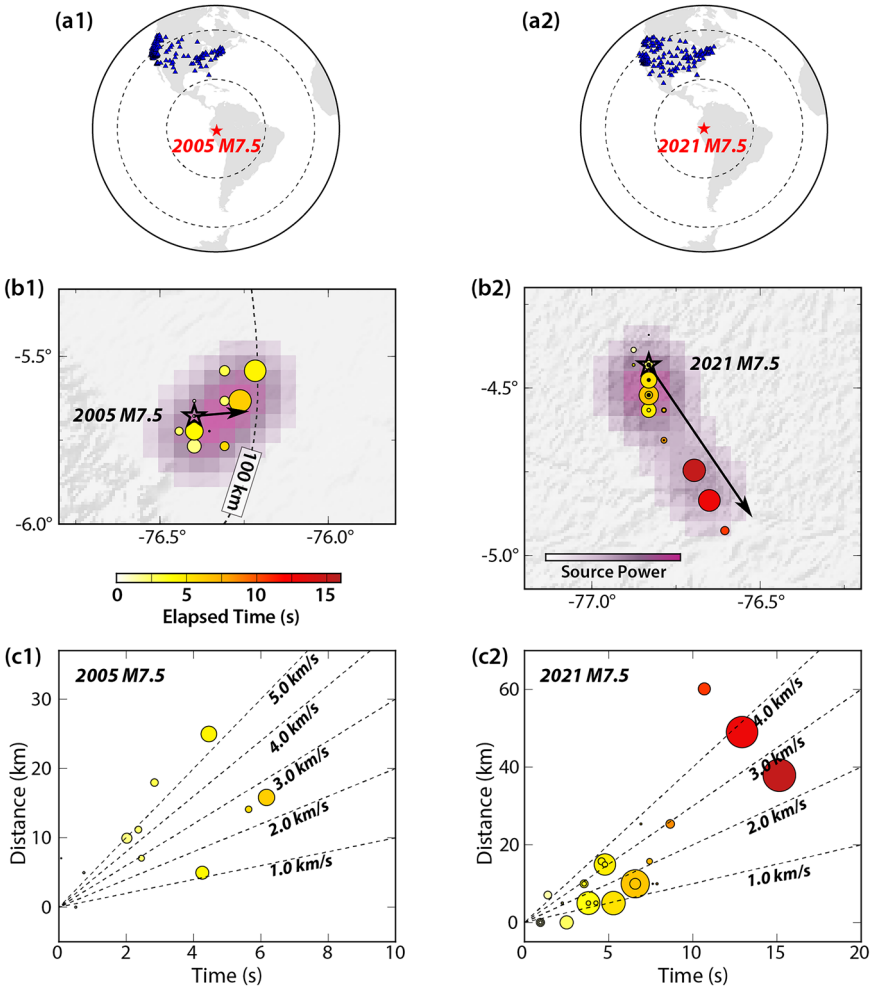

Fig. 3 | Compressive sensing back-projection (CS-BP) analysis of the 2005 M_W 7.5 and 2021 M_W 7.5 earthquakes. a1, **a2** The stations (blue triangles) used for CS-BP analysis in the National Seismic Network. The red stars indicate the epicenters of the 2005 M_W 7.5 and 2021 M_W 7.5 earthquakes. Gray dashed circles show 30° and 60° epicentral distance contours. **b1**, **b2** High frequency (HF; 0.7–2.0 Hz) energy radiation, color-coded with elapsed time. The black stars indicate the epicenters of the 2005 M_W 7.5 and 2021 M_W 7.5 earthquakes. The background purple color scale corresponds to the relative source power. Black arrows indicate the rupture length L_r and reference rupture direction φ_{ref} obtained from directivity analysis (Fig. 2). The gray dashed curve in (**b1**) shows the 100-km slab interface from Slab 2.0[52]. **c1**, **c2** Rupture velocity estimation for the back-projected HF energy radiation (dots color-coded with elapsed time).

at ~2–5 GPa[61]) in the crust. Ferrand[50] correlate the upper-plane seismicity in northern Chile with the transition from chrysotile and lizardite to antigorite, and the lower-plane seismicity with the dehydration of serpentine minerals such as chrysotile and antigorite. These earthquakes may be attributed to dehydration embrittlement (e.g. refs. 7,8) or transformation-driven stress transfer[10]. In general, the normally-dipping segments appear to be hydrous, further supported by the abundant volcanoes in the volcanic arc that require extensive dehydration reactions (Figs. 8a and 9). As the normally-dipping slab segments span a broader range of *P-T* environments, the dehydration embrittlement of multiple hydrous minerals, along with other mechanisms such as thermal runaway[62–64], transformation-driven stress transfer[10,50], as well as stress concentration due to slab bending and unbending[22–27], would potentially lead to the observed continuous and more widespread seismicity distribution.

In contrast, the flat-slab segments in South America may maintain relatively cold, minor-dehydrating and possibly relatively dry environments. Lim et al.[65] observe a high V_S (~4.5–4.7 km s^{-1}) and low V_P/V_S (1.60–1.70) within the overriding mantle above the Peruvian flat-slab segment, gradually transforming to low V_S and high V_P/V_S (1.80-1.85) above the adjacent normally-dipping segments. The high V_S and low V_P/V_S above the flat segment, along with the absence of arc volcanoes (Figs. 8a and 9), suggest limited fluids released from the underthrusting slab. Similarly, Porter et al.[66] find a high V_S continental lithosphere above the Pampean flat slab, suggesting water is not escaping during the flattening of the slab. Wagner et al.[67] also observe relatively low V_P, high V_S, and low V_P/V_S (~1.64-1.74) anomaly above the Pampean flat slab. At depths of ~100-200 km, the V_S decreases with increasing temperature (e.g. ref. 68) and the V_P/V_S increases with increasing temperature or water amount, so the observed anomaly of high V_S and low V_P/V_S probably corresponds to a relatively cold and dry environment. Marot et al.[69] also detect a relatively cold and dry (or slightly hydrated) continental mantle above the dense and relatively dry oceanic lithosphere within the Pampean flat-slab segment, manifested in high V_S and relatively regular V_P/V_S (1.75-1.79). While the relatively dry upper mantle and relatively regular V_P/V_S suggest that the flat-slab segment undergoes limited dehydration reactions, a relatively high V_P/V_S of ~1.80 within the section of the slab at depths less than ~60–70 km indirectly suggests that large amounts of fluids have been released before the slab flattening[65,69]. These results are in agreement with the low water flux at ~150 km depth around the flat-slab segments in northern Peru and central Chile inferred by thermal modeling[70]. All observations collectively suggest relatively cold and relatively dry conditions with limited dehydration reactions within the Peruvian and Pampean flat-slab segments, in contrast to the more hydrated adjacent normally-dipping subduction regions.

Based on the declustered ISC-EHB catalog, we compute the background intraslab seismicity rate (number of *M*4.5+ earthquakes per 10^4km^2) in the flat-slab segments and their adjacent normally-dipping segments, using the depth range of 100–150 km and 35–85 km for the South American and Mexican subduction zones, respectively (Fig. S22 and Table S3). For the flattened portions (avoiding the unbending and re-steepening regions) of the flat-slab segments (F1, F2, F3 in Fig. S22 and Table S3), the seismicity rate is remarkably lower (<10 earthquakes per 10^4km^2), compared to the high seismicity rate (~30 events per 10^4km^2) within the normally-dipping slab segments (N1, N2 in Fig. S22 and Table S3). In these regions, the relatively low earthquake activity compared to normally-dipping slabs (Figs. 8 and S22) indicates that the flat slabs are both under relatively low deviatoric stress and have locally limited ongoing

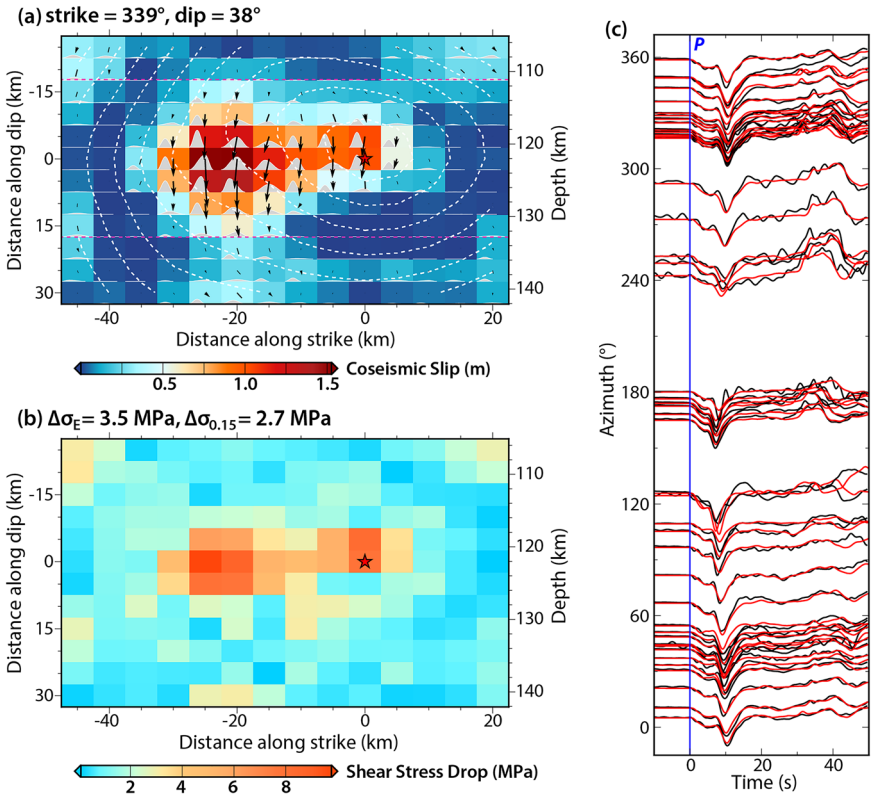

Fig. 4 | Our preferred finite-fault slip model for the 1997 M_W 7.2 earthquake obtained from the inversion of teleseismic *P* wave ground displacements. The red stars in (**a**, **b**) indicate the hypocenter of the 1997 M_W 7.2 earthquake. **a** Slip distribution color-coded with the slip magnitude of each subfault. The size of each subfault is 5 km by 5 km. Black arrows show slip magnitude and direction on each subfault. White dashed contours show rupture fronts with 2-s intervals. Gray triangles indicate the source time function (estimated as a triangle function with a maximum rise time of 4 s) for each subfault. The depth range of the large-slip distribution is estimated with magenta dashed lines. **b** Shear stress drop calculated from this slip model. **c** Comparison of the observed (black) and predicted (red) *P* waveforms produced by this model.

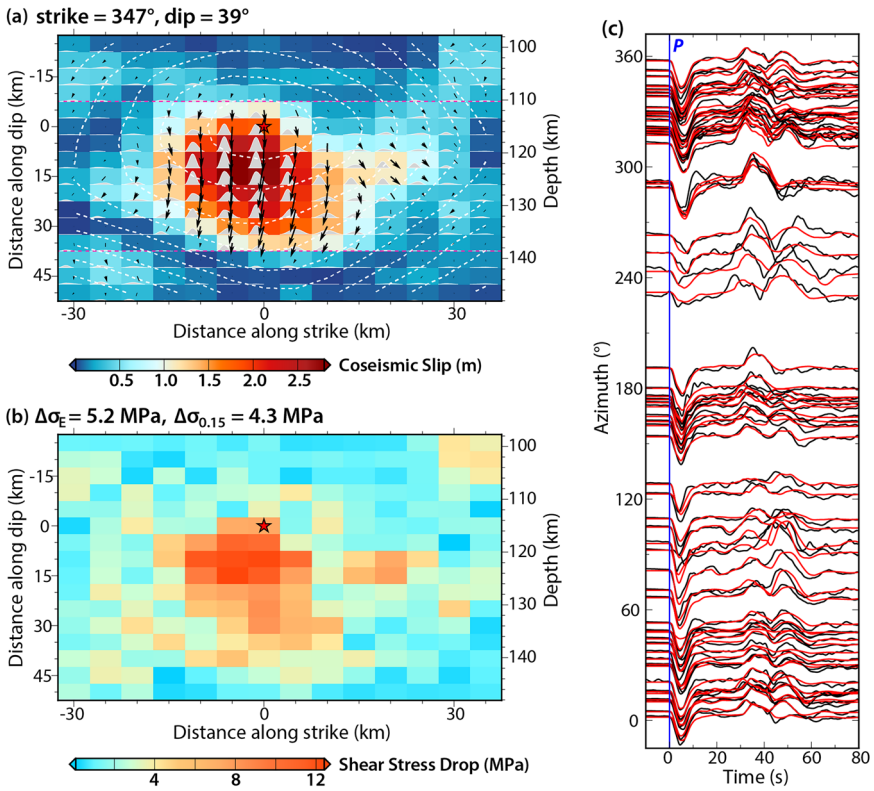

Fig. 5 | Our preferred finite-fault slip model for the 2005 M_W 7.5 earthquake obtained from the inversion of teleseismic *P* wave ground displacements. a Slip distribution. **b** Shear stress drop. **c** Comparison of the observed (black) and predicted (red) *P* waveforms. The red stars in (**a**, **b**) indicate the hypocenter of the 2005 M_W 7.5 earthquake. Layout is the same as in Fig. 4.

dehydration. Dehydration reactions remain potential triggering mechanism for the intraslab earthquakes, but the fractions of hydrous phases are largely limited by the relatively dry flat slabs, and the dehydration reactions are limited by the quasi-stable *P*-*T* conditions within the flat-slab segments. The increase of the seismicity rate at the edge of the flat-slab segments are primarily influenced by the slab stress in the unbending and re-steepening regions, with dehydration reactions possibly contributing to their nucleation (Figs. 8 and S22).

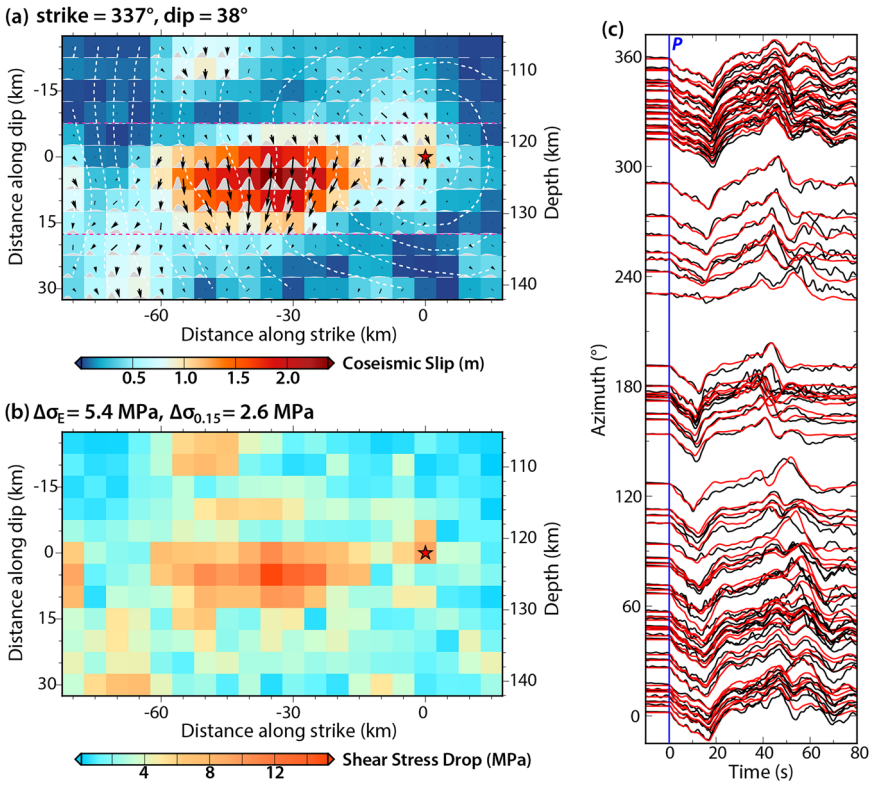

Fig. 6 | Our preferred finite-fault slip model for the 2021 M_W 7.5 earthquake obtained from the inversion of teleseismic *P* wave ground displacements. a Slip distribution. **b** Shear stress drop. **c** Comparison of the observed (black) and predicted (red) *P* waveforms. The red stars in (**a**, **b**) indicate the hypocenter of the 2021 M_W 7.5 earthquake. Layout is the same as in Fig. 4.

The inferred presence of dense, less hydrous minerals may contradict the buoyancy required for slab flattening[69,71]. As the slab descends, the increasing *P-T* conditions prompt interior hydrous minerals to undergo continuous dehydration reactions, eventually transforming basaltic crust to anhydrous eclogite. The eclogitization process within the oceanic crust starts at ~80–90 km depth[8], resulting in increased density which contributes to negative buoyancy that inhibits slab flattening. However, recent numerical models suggest the possibility for short-lived (~10 Myr) flat-slab segments to exist when the subducting slab undergoes a partial eclogitization process for a moderate-size (~200 km long and ~30 km thick) underthrust oceanic plateau[72]. The simulated flattening length of ~200 km and persistence duration of ~10 Myr align well with the Peruvian and Pampean flat-slab segments, which have existed for ~11 Myr and ~12 Myr[73], respectively. Despite the positive buoyancy provided by oceanic plateaus like the Nazca Ridge and the subducted Inca Plateau[74] for the Peruvian flat slab, and the Juan Fernández Ridge for the Pampean flat slab[75], other factors such as craton-wedge suction[76], the overriding plate thickness[76,77], and trench retreat[77] also contribute to the flat-slab subduction, providing support for the viability of dense, less hydrous flat-slab segments. In those flat slabs with limited fluid release, intermediate-depth earthquake faulting can still be triggered by transformation-driven stress transfer[10], amplified differential stresses due to scattered hydrous minerals[25], or plate flexure and eclogitization-related stresses. The stress regimes can cause strain localization[24,78] and trigger shear heating within thin carbonate layers[79] or ultrafine-grained minerals such as dunite, harzburgite, and metamorphosing garnet[64,80], leading to earthquake rupture via thermal runaway instability[62–64].

The spatially offset volcanism above the Mexican flat slab (Figs. 8b and S21) suggests some remaining hydration state persisting through the slab flattening, contrasting with the current volcanic absence above Peruvian and Pampean flat slabs (Figs. 8a and 9). This difference is possibly due to the variation in the slab flattening depth. Arc magmatism primarily originates from partial melting under certain *P-T* conditions in the mantle wedge induced by a flux of slab fluids. Therefore, a crucial factor for arc volcanism is the ability of dehydration fluids to reach the mantle wedge. Thermal models under varying conditions suggest that the water content of the subducting slab decreases as the slab flattening depth increases. According to English et al.[81], a 30–40 Myr old, 600-km long flat slab with a subducting velocity of ~6–8 cm/yr at a flattening depth of ~90 km, comparable to the Peruvian and Pampean flat slabs, likely has a water content of ~0.9–1.1 wt.%. Conversely, at a shallower flattening depth of ~60 km, similar to the Mexican flat slab, it may have a obviously higher water content of ~3.1–6.0 wt.% (Fig. S23). Given these considerations, we interpret that the deep and long Peruvian and Pampean flat-slab segments (~90–100 km depth; Fig. 8a) are relatively low on water content, preventing dehydration fluids from reaching the mantle wedge, resulting in the absence of volcanism above the Peruvian and Pampean flat slabs. Thermal modeling also precludes an arc magmatism source involving flat-slab crustal melting other than in the early stage of pinching out of the overlying mantle wedge, due to difficulties in reaching the necessary melting temperature[82]. In contrast, the shallow and short Mexican flat slab (~40–50 km depth; Fig. 8b) retains higher water content, leading to considerable fluid release and delayed volcanism when the slab re-steepens[28,81]. The lack of volcanism just above the flat segment and the narrow seismicity distribution still suggest limited dehydration within the flat slab beneath Mexico. We hypothesize that the relatively stable pressure conditions in the flat-slab segment may allow hydrous minerals to persist, delaying major dehydration reactions until the slab re-steepens. Further investigation is needed to confirm this hypothesis.

Conceptual model for earthquake faulting in flat- and normally-dipping slab segments

The intermediate-depth intraslab seismicity within the Peruvian, Pampean, and Mexican flat-slab segments evolves with bending and unbending, with large earthquakes concentrated near the slab surface where the subducting plate re-steepens (Fig. 8). Sandiford et al.[15,24] find that the flat-slab seismicity systematically correlates with the curvature gradient of the slab, reflecting the rate of slab bending deformation, with tensional and compressional stresses inferred from focal mechanisms correlating with bending-induced stretching and shortening of the slab, respectively. Within the Peruvian and Pampean flat-slab segment, earthquakes occur in high V_S and low V_P/V_S

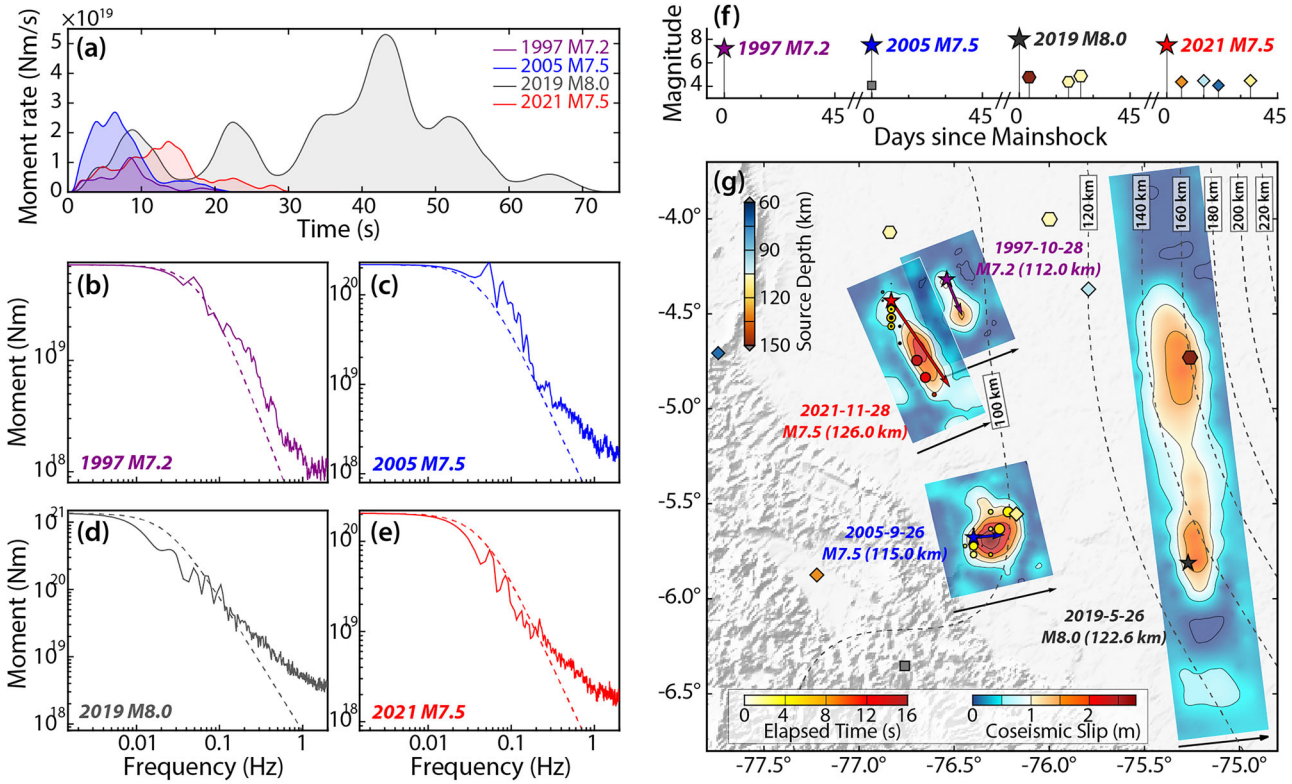

Fig. 7 | Comparison of source models for the major intermediate-depth earthquakes in 1997, 2005, 2019, and 2021. a The moment rate functions for the 1997 M_W 7.2 (purple), 2005 M_W 7.5 (blue), 2019 M_W 8.0 (gray), and 2021 M_W 7.5 (red) earthquakes. Source spectra for **b** 1997 M_W 7.2, **c** 2005 M_W 7.5, **d** 2019 M_W 8.0[21], and **e** 2021 M_W 7.5 earthquakes calculated from the moment rate functions and broadband *P* waveforms, using a seismic attenuation parameter $t^* = 0.75$ s. The dashed curves indicate reference ω^{-2} source spectra. **f** Magnitude-time sequence of the 45-day aftershocks following the major intermediate-depth earthquakes in 1997, 2005, 2019, and 2021. **g** Slip models for the 1997 M_W 7.2, 2005 M_W 7.5, 2019 M_W 8.0[31], and 2021 M_W 7.5 earthquakes, along with the locations of HF radiation bursts (dots color-coded with elapsed time) for the 2005 and 2021 M_W 7.5 earthquakes. The purple, blue, gray, and red stars indicate the epicenters of the mainshocks in 1997, 2005, 2019, and 2021, respectively. The squares, hexagons, and diamonds color-coded with source depths show the locations of aftershocks following the mainshocks in 2005, 2019, and 2021 within 45 days. The purple, blue, and red arrows show the rupture directivities of the mainshocks in 1997, 2005, and 2021, respectively. The thin black arrows beneath the slip models show the dipping directions of our preferred fault planes.

regions with a lack of fluid[65–67,69,83]; the seismicity distribution and stress axes align with the 2D curvature gradient in the Pampean flat slab[84], which reveals the time-independent advective component of strain rates.

Hence, we propose a conceptual model to explain the narrow seismogenic bands of intermediate-depth seismicity within flat-slab segments compared to the widespread seismicity distribution within normal subduction regions (Fig. 10).

(1) In deep and long flat subduction regions, such as the Peruvian and Pampean flat-slab segments (Fig. 10a), the slab flattens at a depth of ~90–100 km below the thick continental lithosphere, leading to low water expulsion from the slab and very little melting. With most fluid released at ~60–70 km depths before the slab flattening[65,69], the relatively less hydrous interior of the flat-slab segment at uniform pressure results in limited or minor dehydration reactions. With no magma formation due to minimal fluid release and no overlying mantle wedge flow, there is absence of volcanoes in the overlying region. Intermediate-depth seismicity primarily results from flexure or high strain rates concentrated shallowly in the slab near where the slab re-steepens. The sparsely distributed seismicity within the minor-dehydrating and relatively dry flat slabs away from the bend could be due to the amplified differential stress from the scattered hydrous phases[25]. Large *M*7+ extensional earthquakes tend to occur on nearly parallel faults near the slab re-steepening sections where strain accumulation is pronounced and relatively uniform. Their rupture propagation is confined to a narrow depth range near the slab surface, consistent with the distribution of background seismicity, suggesting narrow seismogenic bands associated with differential stress induced by plate bending within relatively dry flat-slab segments, or at least with limited dehydration/transformation reactions of minerals due to the quasi-constant pressure conditions associated with flat slabs. We interpret the relatively high radiation efficiencies with low dissipation for those major earthquakes and the lack of aftershocks to be a result of relatively cold and dry conditions.

(2) In shallow and short flat-slab subduction regions, such as the Mexican flat-slab segment (Fig. 10b), the shallow flattening of the slab at ~40–50 km depth and the stable *P*-*T* conditions within the flat segment allows retention of large water content in hydrous phases until the slab re-steepening, resulting in landward-shifted volcanism. Although the subducting slab is not as dry as the deep and long flat segments beneath South America, the similar contrast in seismogenic distribution relative to the normally-dipping subduction regions suggests that the hydrofracturing by dehydration embrittlement may not be the primary mechanism for the intermediate-depth seismicity within the Mexican flat slab. We hypothesize that the major dehydration is delayed in the Mexican flat-slab segment due to the quasi-constant pressure conditions until that fluid flux is enhanced by the near-bend faulting and potentially by the rapid change of dynamic pressure within the slab[55]; this requires further investigation.

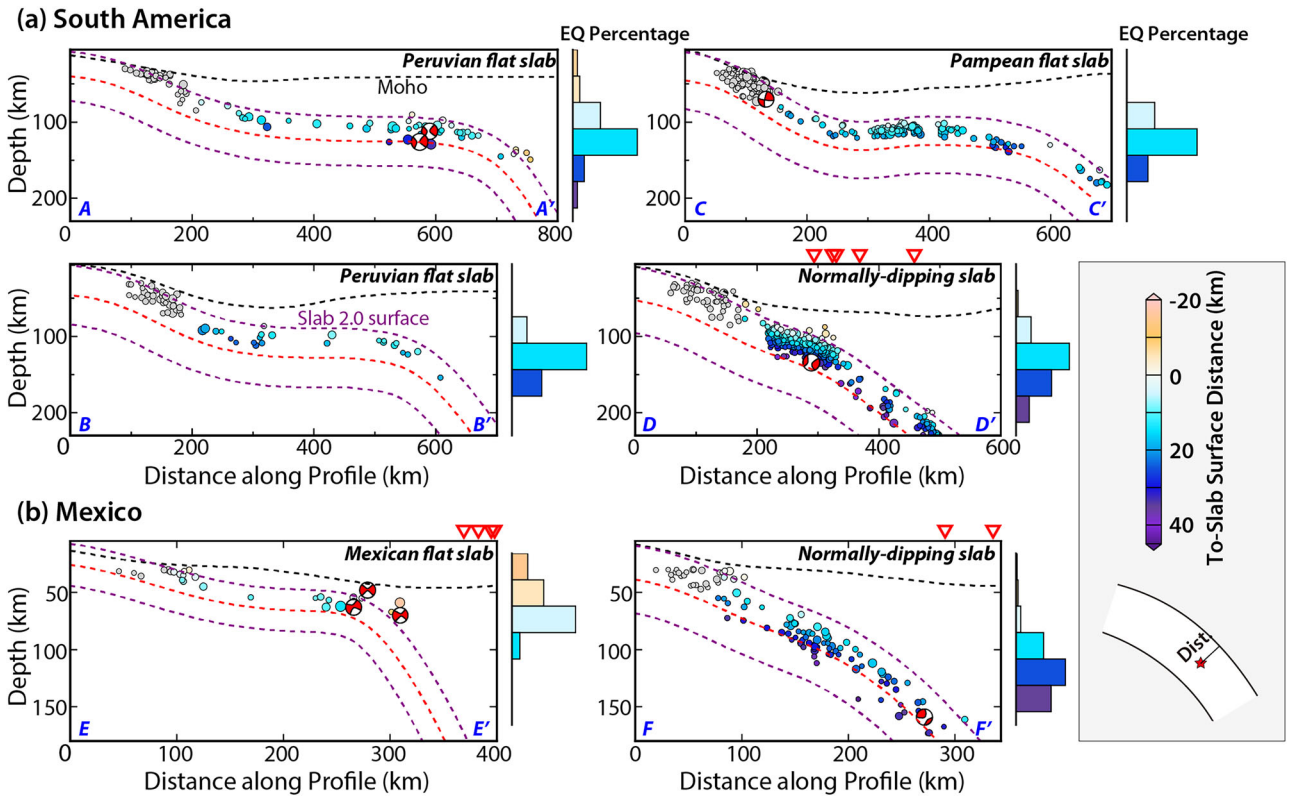

Fig. 8 | Distance from seismicity to the slab surface distributions for subduction regions with flat-slab and normally-dipping segments. a Historical M4.5+ intraslab seismicity including events within 25 km above the proximal slab interface model from 1964 to 2020 (from the declustered ISC-EHB catalog) within profiles AA'-DD' of the South America subduction zone (flat-slab profiles: AA', BB', and CC'; normally-dipping slab profile: DD'; see Figs. 9 and S16 for more information), color-coded with perpendicular distance to the Slab 2.0 interface[52]. The along-strike width of each profile is 150 km. The GCMT focal mechanisms of historical *M*7+ intermediate earthquakes from the USGS-NEIC catalog are shown by the red focal mechanism (vertical cross-sections). Top, middle and bottom slab positions from Slab 2.0[52] are indicated by the purple and red dashed curves, while the upper plate Moho depths from CRUST 1.0 are indicated by the black dashed curves. Red inverted triangles mark the locations of volcanoes. The right-side histograms illustrate the distribution percentage of intraslab in-profile earthquakes (EQ Percentage) in relation to their distance to the subducting slab surface. **b** Historical intraslab seismicity within profiles EE'-FF' of the Mexican subduction zone (flat-slab profile: EE'; normal-slab profile: FF'; see Figs. S17 and S19 for more information).

(3) In the normally-dipping subduction regions, such as the Nazca slab in central South America (Fig. 10c), we observe a more widespread seismicity distribution. The intermediate-depth earthquakes in such subducting slabs are likely triggered by a spectrum of dehydration embrittlement or dehydration-driven stress transformation of multiple minerals under varying *P*-*T* conditions. Fluid flux into the mantle wedge then accounts for the presence of abundant arc volcanism at a conventional distance from the trench.

Methods

Hypocenter relocation

The origin times and hypocenters provided by the USGS catalog are: 28 October 1997 (06:15:17 UTC, 4.368 °S, 76.681 °W, 112.0 km depth), 26 September 2005 (01:55:37 UTC, 5.678 °S, 76.398 °W, 115.0 km depth), and 28 November 2021 (10:52:14 UTC, 4.467 °S, 76.813 °W, 126.0 km depth). We first perform an absolute relocation to determine the 2021 M_W 7.5 earthquake hypocenter using a grid search method, based on the manually-picked arrival times recorded by 205 well-distributed global seismic stations (Fig. S3). The objective function is the L2-norm residual between manually picked *P*-wave arrivals and predicted arrivals using the IASP91 model. The inversion grid spans 100 km in each dimension, with a grid interval of 2 km. The relocated hypocenter is at (4.431°S, 76.831°W) with a depth of 122 km.

Considering the relatively poor data coverage of the 1997 M_W 7.2 earthquake, we relocate this event relative to the adjacent 2021 M_W 7.5 earthquake using the *P*-wave travel time differences. Assuming both events occur at the same (122 km) depth, the travel time difference for the *P* wave at the i^{th} station[85] is

$$\Delta T = T_i^{1997} - T_i^{2021} = T_0 - \gamma_i \Delta L \quad (1)$$

where

$$\gamma_i = p_i \cos(\varphi_i - \Delta\varphi) \quad (2)$$

Here, T_0 is a constant, γ_i is a relative directivity parameter, φ_i is the station azimuth, ΔL and $\Delta\varphi$ are distance and azimuthal difference between the two events. We manually pick the teleseismic *P*-wave onsets of the 1997 and 2021 earthquakes at 37 stations, and perform a grid search for ΔL, $\Delta\varphi$, T_0. We set the station weight based on the azimuth coverage. The result shows that the 1997 event is located at 34.5 km away from the 2021 earthquake in the relative azimuth of 69 ° (Fig. S4), i.e., the relocated epicenter at (4.32 °S, 76.54 °W).

Directivity analysis

The azimuthal distribution of common features in seismograms can directly indicate the direction and extent of the rupture propagation, characterized by the directivity parameter[85]

$$\Gamma = p \cos(\varphi_{sta} - \varphi_{ref}) \quad (3)$$

where p is the ray parameter, φ_{sta} is the station azimuth, and φ_{ref} is the reference rupture direction. For a linear rupture source, the peak arrivals

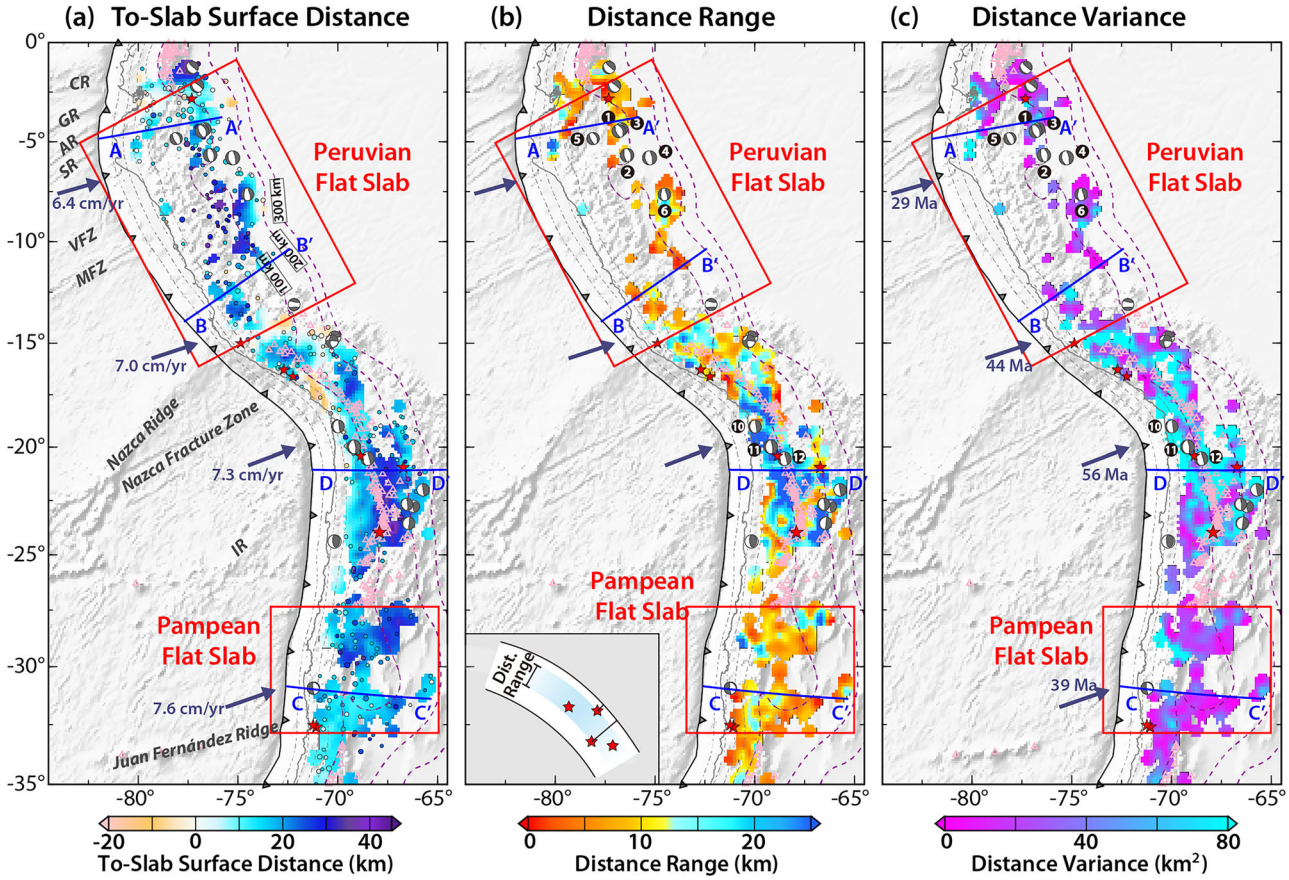

Fig. 9 | Intraslab seismicity-to-slab surface distance analysis for the South American subduction region. a The average, **b** the distribution range, and **c** the distribution variance of the seismicity-to-slab surface distance for the subducting Nazca plate, derived from the M4.5+ intraslab seismicity including events within 25 km above the proximal slab interface model from 1964 to 2020 (from the declustered ISC-EHB catalog; see Figs. S16 and S18). A grid size of 0.3° and an interpolation interval of 0.1° were employed. Pink triangles mark the locations of volcanoes. The flat slab segments are highlighted by the red rectangles. The slab interface depth is provided by Slab 2.0[52] and indicated by the purple dashed curves (at 100-km intervals) and gray dot-dash curves (at 20-km intervals), reaching a maximum depth of 300 km. Blue solid lines represent seismicity profiles AA'-DD' in Fig. 8. The locations of historical *M*7+ intermediate-depth earthquakes from the USGS-NEIC catalog are marked by red stars or gray focal mechanisms (for available GCMT moment tensors). The numbered earthquakes match their schematic depictions in Fig. 10. CR Carnegie Ridge, GR Grijalva Ridge, AR Alvarado Ridge, SR Sarmiento Ridge, VFZ Viru Fracture Zone, MFZ Mendaña Fracture Zone, IR Iquique Ridge.

T^{peak} of teleseismic *P*-wave ground displacement relative to the onset T^{onset} follow the relationship

$$T^{peak} - T^{onset} = \frac{L_r}{V_r} - \Gamma L_r \quad (4)$$

in which L_r is the rupture extent, V_r is the rupture speed. With the global teleseismic data filtered between 0.05 Hz and 10 Hz, we perform a grid search for the rupture extent, direction, and speed of the 1997, 2005, and 2021 Peruvian earthquakes (Figs. S5–S7). The peaks of ground displacements with respect to manually picked *P*-wave onsets show linear trends with the directivity parameter, consistent with parameters from the grid search (Fig. 2).

Compressive sensing back-projection (CS-BP) analysis

We apply the CS-BP analysis[30] to the teleseismic *P*-wave ground velocity data. The waveforms are firstly filtered to a broad frequency band of 0.05–4.0 Hz and aligned by cross-correlation for the first 10 s after the predicted *P*-wave arrivals, in order to suppress the heterogeneous effects in the travel paths. Traces with lower quality (correlation coefficient <0.7 or signal-to-noise ratio <7) are removed, leaving 219 stations for the 2005 event and 243 stations for the 2021 event. Then, we filter data to a high-frequency band of 0.7–2.0 Hz, with a sliding window employed to invert for the spatiotemporal distribution of the subevents, with the length and step of each sliding window of 5 s and 2 s. The source grid covers a 150 km by 150 km area for both events, centered on the epicenter, with a grid interval of 5 km by 5 km. With the waveforms and the propagator matrix transformed to the frequency domain, a sparse inversion is performed to identify the subevents corresponding to the stacked waveforms through a software package http://cvxr.com/CVX. Generally, the HF radiation distributions for the 2005 and 2021 events are in good consistency with the directivity analysis, indicating the robustness of our results. Due to its limited array recordings, we cannot perform the CS-BP analysis for the 1997 event.

Finite-fault inversion

We perform a wavelet-based simulated annealing finite-fault inversion[86] to investigate the coseismic slip distribution of the 1997 M_W 7.2, 2005 M_W 7.5, and 2021 M_W 7.5 Peru earthquakes, using teleseismic *P* wave ground displacement waveforms recorded by global stations within an epicentral distance of 32°–98° (Fig. S9), low-pass filtered below 0.625 Hz. We include the depth phases (*pP* and *sP*) to improve the reliability of slip distributions at depth. We pick the east-dipping planes from the GCMT solutions as the preferred planes, to be consistent with that for the 2019 M_W 8.0 event according to Ye et al.[21]. We set a uniform subfault size of 5 km × 5 km, with each subfault source time function represented by a cosine function. The rising and falling times of the cosine function can vary from 1.0 s to 2.0 s

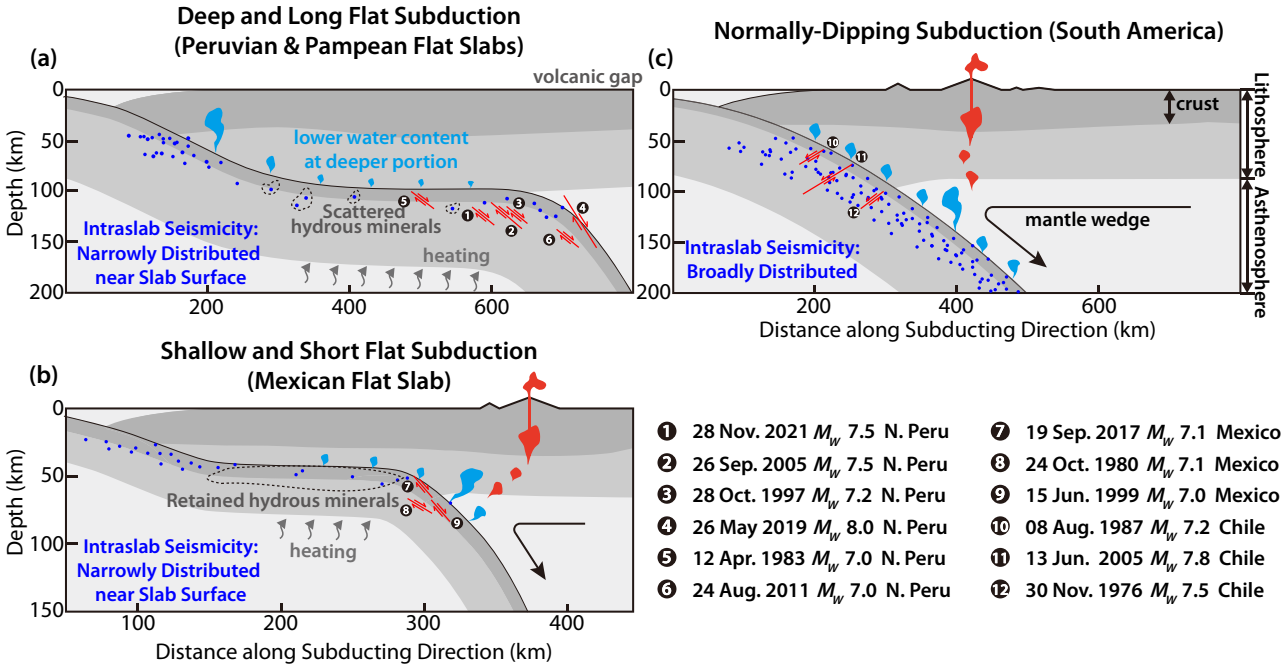

Fig. 10 | Schematic cross-sections of seismicity and slab geometry relationships in different subduction regions. a deep and long flat-slab subduction region (e.g., the Peruvian and Pampean flat slabs), **b** shallow and short flat subduction region (e.g., the Mexican flat slab), and **c** normally-dipping subduction region (e.g., South America). Blue dots indicate intraslab seismicity. Historical *M*7+ intermediate-depth earthquakes associated with flat and normal subductions since 1976 are marked with numbers (see Figs. 9 and S19 for more information).

with a step of 0.5 s, allowing for a total subfault rupture duration from 2.0 s to 4.0 s. Guided by the directivity and CS-BP analysis, the reference rupture propagation speeds are set as 2.6 km s^{-1}, 3.7 km s^{-1}, and 3.5 km s^{-1} for the 1997, 2005, and 2021 events, respectively. Results on the alternative planes are presented in the supplementary materials (Figs. S10–S13), which show that major slip patches are confined to be within a narrow depth range.

Shear stress change

We calculate the slip-weighted stress drop using the finite-fault models following Ye et al.[34]. The stress change is firstly calculated for each subfault, and the average stress change is weighted by the slip distribution,

$$\Delta\sigma_E = \frac{\int \Delta\sigma_1 \Delta u_1 dS}{\int \Delta u_1 dS} \quad (5)$$

where $\Delta\sigma_1$ and Δu_1 are stress change and slip on each subfault, respectively. The slip-weighted stress drop are 3.5 MPa, 5.2 MPa, and 5.4 MPa for the 1997, 2005, and 2021 earthquakes, respectively, comparable to that of 5.2 MPa for the 2019 M_W 8.0 event[21].

Source spectra and radiated energy

We calculate the source spectra for the 1997, 2005, and 2021 Peruvian earthquakes by combining the lower frequency (<0.05 Hz) spectra of moment rate functions from our finite-fault inversions and stacked higher frequency (>0.05 Hz) spectra of broadband *P* waveforms with the seismic attenuation parameter set to $t^* = 0.75$ s. The source spectrum for the 2019 earthquake is from Ye et al.[21].

Radiated energy E_R, calculated from the source spectra up to 2 Hz, are 2.4×10^{15} J, 1.0×10^{16} J, and 4.5×10^{15} J for the 1997, 2005, and 2021 earthquakes, respectively. Using the seismic moment from the GCMT catalog, the corresponding moment-scaled radiated energy are 3.3×10^{-5}, 4.7×10^{-5}, and 2.2×10^{-5}, comparable to that of 2.3×10^{-5} for the 2019 M_W 8.0 event (Ye et al.[21]).

Seismicity distribution analysis

We analyze the distribution of intermediate-depth seismicity in subducting slabs beneath South America and Mexico using the ISC-EHB catalog. This catalog provides relocated hypocenters for the earthquakes occurring from 1964 to 2020 with relatively well-constrained source depths with depth phases. We focus on the intraslab seismicity above the completeness magnitude[87] of *M*4.5 (Fig. S15) separating from the megathrust earthquakes, below the 60 km depth for the subducting Nazca plate (the Peruvian and Pampean flat-slab segments; Fig. S16) and below the 30 km depth for the Cocos plate (the Mexican flat-slab segment; Fig. S17). We then apply the declustering method based on the Nearest-Neighbor Distance Algorithm[88] (Fig. S18) to the selected catalog, with corresponding thresholds shown in Table S2. The final patterns are robust whether using this declustered catalog or using the original ISC-EHB catalog, indicating that our observed seismicity distribution does not depend on declustering.

We calculate the seismicity-to-slab surface distance as the minimum distance between the earthquake and the nearby slab surface within a radius of 0.25°. The slab surface is from the Slab 2.0[52] interpolated at a 0.01° interval. The subduction zone is divided into uniform square grids of 0.3° (Figs. S20–S21, a1–a3), with the average seismicity-to-slab surface distance and its distribution range for multiple earthquakes calculated for each grid. If there is only one earthquake in the grid, we plot it as an individual event (a circle). The gridded data are then interpolated at a 0.1° interval with a smoothing radius of 0.1° (Figs. 9 and S20).

A larger grid size of 0.6° has also been applied to the averaging and smoothing processes for the South American subduction region (Fig. S20) and the Mexican subduction region (Fig. S21), respectively. The seismicity distributions in flat-slab and adjacent normally-dipping slab segments remain distinct, with similar patterns observed in the range and variance of seismicity-to-slab surface distance.

Data availability

All data used in this study are openly available online. Earthquake catalogs are from the USGS-NEIC (https://www.usgs.gov/programs/earthquake-hazards/earthquakes) and ISC-EHB bulletin (https://www.isc.ac.uk/isc-

ehb). The focal mechanisms are from the Global Centroid Moment Tensor solutions (https://www.globalcmt.org[89,90]). The teleseismic data were downloaded from the Incorporated Research Institutions for Seismology (IRIS) data management center (http://ds.iris.edu/wilber3/find_event). Volcanism data is from the Smithsonian Institution's Global Volcanism Program (https://volcano.si.edu/). Seafloor age data are from the global data set contributed by Seton et al. (https://earthbyte.org/webdav/ftp/earthbyte/agegrid/2020/). The plate motion data are provided by the NNR-MORVEL56 model (http://www.geology.wisc.edu/~chuck/MORVEL/). The Moho depths are from CRUST 1.0 (https://igppweb.ucsd.edu/~gabi/crust1.html). All links were last accessed on September 13, 2024.

Code availability

The custom codes used in this study are available upon request to Lingci Zeng (zenglc@mail.ustc.edu.cn) and Lingling Ye (yell@sustech.edu.cn).

Received: 6 May 2024; Accepted: 28 January 2025;
Published online: 12 February 2025

References

1. Benioff, H. Orogenesis and deep crustal structure—additional evidence from seismology. *Geol. Soc. Am. Bull.* **65**, 385–400 (1954).
2. Sykes, L. R. The seismicity and deep structure of island arcs. *J. Geophys. Res.* **71**, 2981–3006 (1966).
3. Isacks, B. & Molnar, P. Distribution of stresses in the descending lithosphere from a global survey of focal-mechanism solutions of mantle earthquakes. *Rev. Geophys.* **9**, 103–174 (1971).
4. Isacks, B. & Molnar, P. Mantle earthquake mechanisms and the sinking of the lithosphere. *Nature* **223**, 1121–1124 (1969).
5. Forsyth, D. & Uyeda, S. On the relative importance of the driving forces of plate motion. *Geophys. J. Int.* **43**, 163–200 (1975).
6. Kirby, S., Engdahl, R. E. & Denlinger, R. Intermediate-depth intraslab earthquakes and arc volcanism as physical expressions of crustal and uppermost mantle metamorphism in subducting slabs. *Geoph. Monog. Se.* **96**, 195–214 (1996).
7. Peacock, S. M. Are the lower planes of double seismic zones caused by serpentine dehydration in subducting oceanic mantle? *Geology* **29**, 299–302 (2001).
8. Hacker, B. R., Peacock, S. M., Abers, G. A., & Holloway, S. D. Subduction factory 2. Are intermediate-depth earthquakes in subducting slabs linked to metamorphic dehydration reactions? *J. Geophys. Res.: Solid Earth* **108**, 2030 (2003).
9. Jung, H., Green, H. W. II & Dobrzhinetskaya, L. F. Intermediate-depth earthquake faulting by dehydration embrittlement with negative volume change. *Nature* **428**, 545–549 (2004).
10. Ferrand, T. P. et al. Dehydration-driven stress transfer triggers intermediate-depth earthquakes. *Nat. Commun.* **8**, 15247 (2017).
11. Raleigh, C. B. & Paterson, M. S. Experimental deformation of serpentinite and its tectonic implications. *J. Geophys. Res.* **70**, 3965–3985 (1965).
12. Comte, D. et al. A double-layered seismic zone in Arica, northern Chile. *Geophys. Res. Lett.* **26**, 1965–1968 (1999).
13. Kumar, A. et al. Seismicity and state of stress in the central and southern Peruvian flat slab. *Earth Planet. Sci. Lett.* **441**, 71–80 (2016).
14. Melgar, D. et al. Bend faulting at the edge of a flat slab: The 2017 Mw7. 1 Puebla-Morelos, Mexico earthquake. *Geophys. Res. Lett.* **45**, 2633–2641 (2018).
15. Sandiford, D., Moresi, L., Sandiford, M. & Yang, T. Geometric controls on flat slab seismicity. *Earth Planet. Sci. Lett.* **527**, 115787 (2019).
16. Beck, S., Barrientos, S., Kausel, E. & Reyes, M. Source characteristics of historic earthquakes along the central Chile subduction Askew et Alzone. *J. South Am. Earth Sci.* **11**, 115–129 (1998).
17. Okuwaki, R. & Yagi, Y. Rupture process during the *Mw* 8.1 2017 Chiapas Mexico earthquake: Shallow intraplate normal faulting by slab bending. *Geophys. Res. Lett.* **44**, 11–816 (2017).
18. Ye, L., Lay, T., Bai, Y., Cheung, K. F. & Kanamori, H. The 2017 Mw 8.2 Chiapas, Mexico, earthquake: energetic slab detachment. *Geophys. Res. Lett.* **44**, 11–824 (2017).
19. Ye, L., Lay, T. & Kanamori, H. The 23 June 2014 Mw 7.9 Rat Islands archipelago, Alaska, intermediate depth earthquake. *Geophys. Res. Lett.* **41**, 6389–6395 (2014).
20. Twardzik, C. & Ji, C. The Mw7.9 2014 intraplate intermediate-depth Rat Islands earthquake and its relation to regional tectonics. *Earth Planet. Sci. Lett.* **431**, 26–35 (2015).
21. Ye, L., Lay, T. & Kanamori, H. Anomalously low aftershock productivity of the 2019 Mw 8.0 energetic intermediate-depth faulting beneath Peru. *Earth Planet. Sci. Lett.* **549**, 116528 (2020).
22. Engdahl, E. R. & Scholz, C. H. A double Benioff zone beneath the central Aleutians: an unbending of the lithosphere. *Geophys. Res. Lett.* **4**, 473–476 (1977).
23. Sleep, N. H. The double seismic zone in downgoing slabs and the viscosity of the mesosphere. *J. Geophys. Res. Solid Earth* **84**, 4565–4571 (1979).
24. Sandiford, D., Moresi, L. M., Sandiford, M., Farrington, R. & Yang, T. The fingerprints of flexure in slab seismicity. *Tectonics* **39**, e2019TC005894 (2020).
25. Toffol, G., Yang, J., Pennacchioni, G., Faccenda, M. & Scambelluri, M. How to quake a subducting dry slab at intermediate depths: Inferences from numerical modelling. *Earth Planet. Sci. Lett.* **578**, 117289 (2022).
26. Craig, T. J., Methley, P. & Sandiford, D. Imbalanced moment release within subducting plates during initial bending and unbending. *J. Geophys. Res. Solid Earth* **127**, e2021JB023658 (2022).
27. Sippl, C., Dielforder, A., John, T. & Schmalholz, S. M. Global constraints on intermediate-depth intraslab stresses from slab geometries and mechanisms of double seismic zone earthquakes. *Geochem. Geophys. Geosyst.* **23**, e2022GC010498 (2022).
28. Manea, V. C. & Manea, M. Flat-slab thermal structure and evolution beneath central Mexico. *Pure Appl. Geophys.* **168**, 1475–1487 (2011).
29. Barazangi, M. & Isacks, B. L. Subduction of the Nazca plate beneath Peru: evidence from spatial distribution of earthquakes. *Geophys. J. Int.* **57**, 537–555 (1979).
30. Yao, H., Gerstoft, P., Shearer, P. M., & Mecklenbräuker, C. Compressive sensing of the Tohoku-Oki Mw 9.0 earthquake: frequency-dependent rupture modes. *Geophys. Res. Lett*. **38**, L20310 (2011).
31. Liu, W. & Yao, H. Rupture process of the 26 May 2019 Mw 8.0 northern Peru intermediate-depth earthquake and insights into its mechanism. *Geophys. Res. Lett.* **47**, e2020GL087167 (2020).
32. Luo, H. et al. Could thermal pressurization have induced the frequency-dependent rupture during the 2019 Mw 8.0 Peru intermediate-depth earthquake? *Geophys. J. Int* **232**, 115–127 (2023).
33. Vallée, M. et al. Self-reactivated rupture during the 2019 Mw= 8 northern Peru intraslab earthquake. *Earth Planet. Sci. Lett.* **601**, 117886 (2023).
34. Ye, L., Lay, T., Kanamori, H. & Rivera, L. Rupture characteristics of major and great (Mw≥ 7.0) megathrust earthquakes from 1990 to 2015: 1. Source parameter scaling relationships. *J. Geophys. Res.: Solid Earth* **121**, 826–844 (2016).
35. Ye, L., Lay, T., Kanamori, H., Freymueller, J. T. & Rivera, L. Joint inversion of high-rate GPS and teleseismic observations for rupture process of the 23 June 2014 (Mw 7.9) Rat Islands archipelago, Alaska, intermediate depth earthquake. In *Plate Boundaries and Nature Hazards*, 149–166 (American Geophysical Union, 2016).
36. Ye, L., Lay, T., Kanamori, H., Zhan, Z. & Duputel, Z. Diverse rupture processes in the 2015 Peru deep earthquake doublet. *Sci. Adv.* **2**, e1600581 (2016).
37. Derode, B. & Campos, J. Energy budget of intermediate-depth earthquakes in northern Chile: comparison with shallow earthquakes and implications of rupture velocity models used. *Geophys. Res. Lett.* **46**, 2484–2493 (2019).

38. Poli, P. & Prieto, G. A. Global rupture parameters for deep and intermediate-depth earthquakes. *J. Geophys. Res. Solid Earth* **121**, 8871–8887 (2016).
39. Prieto, G. A. et al. Seismic evidence for thermal runaway during intermediate-depth earthquake rupture. *Geophys. Res. Lett.* **40**, 6064–6068 (2013).
40. Wei, S. S., Wiens, D. A., van Keken, P. E. & Cai, C. Slab temperature controls on the Tonga double seismic zone and slab mantle dehydration. *Sci. Adv.* **3**, e1601755 (2017).
41. Wiens, D. A. & Gilbert, H. J. Effect of slab temperature on deep-earthquake aftershock productivity and magnitude-frequency relations. *Nature* **384**, 153–156 (1996).
42. Wortel, R. Seismicity and rheology of subducted slabs. *Nature* **296**, 553–556 (1982).
43. Anderson, D. L. Lithosphere, asthenosphere, and perisphere. *Rev. Geophys.* **33**, 125–149 (1995).
44. Araya Vargas, J., Sanhueza, J. & Yáñez, G. The role of temperature in the along-margin distribution of volcanism and seismicity in subduction zones: insights from 3-D thermomechanical modeling of the Central Andean margin. *Tectonics* **40**, e2021TC006879 (2021).
45. Hasegawa, A., Umino, N. & Takagi, A. Double-planed structure of the deep seismic zone in the northeastern Japan arc. *Tectonophysics* **47**, 43–58 (1978).
46. Brudzinski, M. R., Thurber, C. H., Hacker, B. R. & Engdahl, E. R. Global prevalence of double Benioff zones. *Science* **316**, 1472–1474 (2007).
47. Florez, M. A. & Prieto, G. A. Precise relative earthquake depth determination using array processing techniques. *J. Geophys. Res. Solid Earth* **122**, 4559–4571 (2017).
48. Yamasaki, T., & Seno, T. Double seismic zone and dehydration embrittlement of the subducting slab. *J. Geophys. Res. Solid Earth* **108**, 2212 (2003).
49. Abers, G. A., Nakajima, J., van Keken, P. E., Kita, S. & Hacker, B. R. Thermal–petrological controls on the location of earthquakes within subducting plates. *Earth Planet. Sci. Lett.* **369**, 178–187 (2013).
50. Ferrand, T. P. Seismicity and mineral destabilizations in the subducting mantle up to 6 GPa, 200 km depth. *Lithos* **334**, 205–230 (2019).
51. Reynard, B., Nakajima, J. & Kawakatsu, H. Earthquakes and plastic deformation of anhydrous slab mantle in double Wadati-Benioff zones. *Geophys. Res. Lett.* **37**, 2010GL045494 (2010).
52. Hayes, G. P. et al. Slab2, a comprehensive subduction zone geometry model. *Science* **362**, 58–61 (2018).
53. Ferrand, T. P. & Manea, E. F. Dehydration-induced earthquakes identified in a subducted oceanic slab beneath Vrancea, Romania. *Sci. Rep.* **11**, 10315 (2021).
54. Craiu, A. et al. A switch from horizontal compression to vertical extension in the Vrancea slab explained by the volume reduction of serpentine dehydration. *Sci. Rep.* **12**, 22320 (2022).
55. Faccenda, M., Gerya, T. V., Mancktelow, N. S. & Moresi, L. Fluid flow during slab unbending and dehydration: Implications for intermediate-depth seismicity, slab weakening and deep water recycling. *Geochem. Geophys. Geosyst*. **13**, Q01010 (2012).
56. Cabrera, L. et al. Northern Chile intermediate-depth earthquakes controlled by plate hydration. *Geophys. J. Int* **226**, 78–90 (2021).
57. Sippl, C., Schurr, B., Asch, G. & Kummerow, J. Seismicity structure of the northern Chile forearc from >100,000 double-difference relocated hypocenters. *J. Geophys. Res. Solid Earth* **123**, 4063–4087 (2018).
58. Dorbath, C., Gerbault, M., Carlier, G., & Guiraud, M. Double seismic zone of the Nazca plate in northern Chile: High-resolution velocity structure, petrological implications, and thermomechanical modeling. *Geochem. Geophys. Geosyst*. **9**, Q07006 (2008).
59. Pawley, A. R. & Wood, B. J. The high-pressure stability of talc and 10 Å phase: potential storage sites for H2O in subduction zones. *Am. Min.* **80**, 998–1003 (1995).
60. Pawley, A. Chlorite stability in mantle peridotite: the reaction clinochlore+enstatite=forsterite+pyrope+H2O. *Contrib. Mineral. Petrol.* **144**, 449–456 (2003).
61. Okazaki, K. & Hirth, G. Dehydration of lawsonite could directly trigger earthquakes in subducting oceanic crust. *Nature* **530**, 81–84 (2016).
62. Kelemen, P. B. & Hirth, G. A periodic shear-heating mechanism for intermediate-depth earthquakes in the mantle. *Nature* **446**, 787–790 (2007).
63. John, T. et al. Generation of intermediate-depth earthquakes by self-localizing thermal runaway. *Nat. Geosci.* **2**, 137–140 (2009).
64. Ohuchi, T. et al. Intermediate-depth earthquakes linked to localized heating in dunite and harzburgite. *Nat. Geosci.* **10**, 771–776 (2017).
65. Lim, H., Kim, Y., Clayton, R. W. & Thurber, C. H. Seismicity and structure of Nazca Plate subduction zone in southern Peru. *Earth Planet. Sci. Lett.* **498**, 334–347 (2018).
66. Porter, R. et al. Shear wave velocities in the Pampean flat-slab region from Rayleigh wave tomography: Implications for slab and upper mantle hydration. *J. Geophys. Res. Solid Earth* **117**, B11301 (2012).
67. Wagner, L. S., Beck, S., Zandt, G. & Ducea, M. N. Depleted lithosphere, cold, trapped asthenosphere, and frozen melt puddles above the flat slab in central Chile and Argentina. *Earth Planet. Sci. Lett.* **245**, 289–301 (2006).
68. Priestley, K. & McKenzie, D. The relationship between shear wave velocity, temperature, attenuation and viscosity in the shallow part of the mantle. *Earth Planet. Sci. Lett.* **381**, 78–91 (2013).
69. Marot, M. et al. Flat versus normal subduction zones: a comparison based on 3-D regional traveltime tomography and petrological modelling of central Chile and western Argentina (29-35°S). *Geophys. J. Int* **199**, 1633–1654 (2014).
70. van Keken, P. E., Hacker, B. R., Syracuse, E. M., & Abers, G. A. Subduction factory: 4. Depth-dependent flux of H2O from subducting slabs worldwide. *J. Geophys. Res. Solid Earth* **116**, B01401 (2011).
71. Manea, V. C. et al. A review of the geodynamic evolution of flat slab subduction in Mexico, Peru, and Chile. *Tectonophysics* **695**, 27–52 (2017).
72. Yan, Z. et al. The fate of oceanic plateaus: subduction versus accretion. *Geophys. J. Int* **231**, 1349–1362 (2022).
73. Ramos, V. A. & Folguera, A. Andean flat-slab subduction through time. *Geol. Soc. Spec. Publ* **327**, 31–54 (2009).
74. Rosenbaum, G. et al. Subduction of the Nazca Ridge and the Inca Plateau: Insights into the formation of ore deposits in Peru. *Earth Planet. Sci. Lett.* **239**, 18–32 (2005).
75. Nur, A. & Ben-Avraham, Z. Volcanic gaps and the consumption of aseismic ridges in South America. *Mem. Geol. Soc. Amer.***154**, 729–740 (1981).
76. Manea, V. C., Pérez-Gussinyé, M. & Manea, M. Chilean flat slab subduction controlled by overriding plate thickness and trench rollback. *Geology* **40**, 35–38 (2012).
77. Salze, M. et al. Trench-parallel spreading ridge subduction and its consequences for the geological evolution of the overriding plate: Insights from analogue models and comparison with the Neogene subduction beneath Patagonia. *Tectonophysics* **737**, 27–39 (2018).
78. Nakajima, J. et al. Intermediate-depth earthquakes facilitated by eclogitization-related stresses. *Geology* **41**, 659–662 (2013).
79. Prakash, A. et al. Carbonates and intermediate-depth seismicity: Stable and unstable shear in altered subducting plates and overlying mantle. *Proc. Natl. Acad. Sci.USA* **120**, e2219076120 (2023).
80. Shi, F. et al. Metamorphism-facilitated faulting in deforming orthopyroxene: Implications for global intermediate-depth seismicity. *Proc. Natl. Acad. Sci. USA* **119**, e2112386119 (2022).
81. English, J. M., Johnston, S. T. & Wang, K. Thermal modelling of the Laramide orogeny: testing the flat-slab subduction hypothesis. *Earth Planet. Sci. Lett.* **214**, 619–632 (2003).
82. Gutscher, M. A., Maury, R., Eissen, J. P. & Bourdon, E. Can slab melting be caused by flat subduction? *Geology* **28**, 535–538 (2000).

83. Ma, Y. & Clayton, R. W. The crust and uppermost mantle structure of Southern Peru from ambient noise and earthquake surface wave analysis. *Earth Planet. Sci. Lett.* **395**, 61–70 (2014).
84. Rodriguez Piceda, C. et al. The influence of mantle hydration and flexure on slab seismicity in the southern Central Andes. *Commun. Earth Environ.* **4**, 79 (2023).
85. Ye, L., Lay, T., Zhan, Z., Kanamori, H. & Hao, J. L. The isolated ~680 km deep 30 may 2015 Mw 7.9 Ogasawara (Bonin) Islands earthquake. *Earth Planet. Sci. Lett.* **433**, 169–179 (2016).
86. Ji, C., Wald, D. J. & Helmberger, D. V. Source description of the 1999 Hector Mine, California, earthquake, part II: cComplexity of slip history. *Bull. Seismol. Soc. Am.* **92**, 1208–1226 (2002).
87. Wiemer, S. & Katsumata, K. Spatial variability of seismicity parameters in aftershock zones. *J. Geophys. Res. Solid Earth* **104**, 13135–13151 (1999).
88. Zaliapin, I. & Ben-Zion, Y. Earthquake declustering using the nearest-neighbor approach in space-time-magnitude domain. *J. Geophys. Res. Solid Earth* **125**, e2018JB017120 (2020).
89. Dziewonski, A. M., Chou, T.-A. & Woodhouse, J. H. Determination of earthquake source parameters from waveform data for studies of global and regional seismicity. *J. Geophys. Res.* **86**, 2825–2852 (1981).
90. Ekström, G., Nettles, M. & Dziewonski, A. M. The global CMT project 2004-2010: Centroid-moment tensors for 13,017 earthquakes. *Phys. Earth Planet. Inter.* **200-201**, 1–9 (2012).

Acknowledgements

We thank Emily Brodsky, Shiqing Xu, and Hongfeng Yang for helpful discussion. Helpful reviews were provided by T.P. Ferrand and three anonymous reviewers. The work was supported in part by National Natural Science Foundation of China 42488301 (H.Y.), National Key R&D Program of China 2023YFF0803200 and National Natural Science Foundation of China 42474077 (L.Y.), and National Science Foundation Grant EAR1802364 (T.L.).

Author contributions

L.Z., L.Y., and H.Y. conceived the project; L.Z. and L.Y. conducted most data analysis and wrote the original draft; W.L. helped develop the source inversion code; D.S. calculated the source spectra; L.Z., L.Y., T.L., and T.Y. discussed the volcanism distribution; All coauthors wrote and revised the manuscript collaboratively.

Competing interests

The authors declare no competing interests.

Additional information

Supplementary information The online version contains supplementary material available at https://doi.org/10.1038/s43247-025-02071-0.

Correspondence and requests for materials should be addressed to Lingling Ye or Huajian Yao.

Peer review information *Communications Earth & Environment* thanks Thomas Ferrand and the other, anonymous, reviewer(s) for their contribution to the peer review of this work. Primary Handling Editor: Joe Aslin. A peer review file is available.